Journal of Applied Mechanics and Technical Physics, Vol. 38, No. 1, 1997

APPLICATION OF THE NEWTON METHOD TO THE CALCULATION OF INTERNAL SUPERSONIC SEPARATED FLOWS

V. A. Bashkin, I. V. Yegorov, and D. V. Ivanov

UDC 519.6: 532.5

The method of [1] for numerical integration of the two-dimensional Navier–Stokes and Euler equations is extended to the solution of problems of internal aerodynamics. A technique for generating a refined computation grid in boundary-layer regions depending on the Reynolds number is developed. Calculations of the supersonic flow of a perfect gas in a flat duct of variable cross section are performed. The effect of the Reynolds number on the structure of the flow field and heat exchange is shown.

The development of aerospace technology has attracted considerable attention to the application of supersonic flows to problems of external aerodynamics and to the development of effective methods of their numerical analysis. The Euler or Navier–Stokes equations are commonly used to describe the flow field of incompressible and compressible fluids within the framework of fluid dynamics. By virtue of the nonlinearity of these partial differential equations, their solution can be obtained only by methods of computational aerodynamics. In particular, an effective method of numerical integration of the two-dimensional Navier–Stokes equations in the presence of flow separation and reattachment is proposed by Egorov and Zaitsev [1]. This method is based on implicit monotone second-order difference schemes and on the modified Newton method for solving grid equations. This method was used in studies of some problems related to the supersonic or hypersonic flow of a perfect gas [2, 3] or nonequilibrium air [4, 5] past blunt bodies and also in studies of supersonic flows of an inviscid gas.

Great interest in the investigations of internal supersonic flows has been stimulated by the development of hypersonic air jet engines. Problems of internal aerodynamics have their specific features, and, therefore, the numerical algorithm of solution of the Euler and Navier–Stokes equations requires some modification and adaptation to simulate internal supersonic flows. The algorithm developed in [1] was extended in [6] to internal flows of a perfect gas at moderate Reynolds numbers. Here primary emphasis was placed on computation grid generation by an integral method using the Schwarz–Christoffel integral. Extensive studies on the effect of some governing parameters of the difference scheme on the solution of the Euler and Navier–Stokes equations have also been performed in [6].

In the present paper, this method is further extended to the calculation of supersonic internal flows at high Reynolds numbers Re. The problem of constructing a refined computation grid in the boundary-layer regions is given particular emphasis. The problem becomes more important as Re increases. The effectiveness of our package of programs is tested by calculating the supersonic flow of a perfect gas in a duct of variable cross section over a wide range of Re.

1. In arbitrary curvilinear coordinates ξ, η [$x = x(\xi, \eta)$ and $y = (\xi, \eta)$ are Cartesian coordinates], the unsteady two-dimensional Euler and Navier–Stokes equations are written in nondimensional variables in divergence form as

$$\frac{\partial \mathbf{Q}}{\partial t} + \frac{\partial \mathbf{E}}{\partial \xi} + \frac{\partial \mathbf{G}}{\partial \eta} = 0. \tag{1.1}$$

Here the vectors $\mathbf{Q}$, $\mathbf{E}$, and $\mathbf{G}$ are related to the corresponding Cartesian vectors $\mathbf{Q}_1$, $\mathbf{E}_1$, and $\mathbf{G}_1$ by the formulas $\mathbf{Q} = J\mathbf{Q}_1$, $\mathbf{E} = J(\mathbf{E}_1\partial\xi/\partial x + \mathbf{G}_1\partial\xi/\partial y)$, and $\mathbf{G} = J(\mathbf{E}_1\partial\eta/\partial x + \mathbf{G}_1\partial\eta/\partial y)$, where $J = \partial(x, y)/\partial(\xi, \eta)$ is the Jacobian of the transformation.

Central Aerohydrodynamic Institute, Zhukovskii 140160. Translated from Prikladnaya Mekhanika i Tekhnicheskaya Fizika, Vol. 38, No. 1, pp. 30–42, January–February, 1997. Original article submitted July 21, 1995; revision submitted September 25, 1995.

 0021-8944/97/3801-0026 $18.00

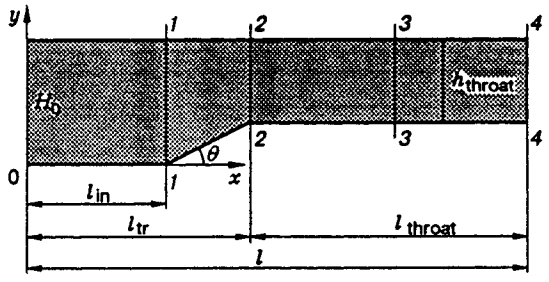

Fig. 1

The Cartesian components of the vectors $\mathbf{Q}_1$, $\mathbf{E}_1$, $\mathbf{G}_1$ for the two-dimensional Euler equations have the form

$$\mathbf{E}_1 = \left| \begin{array}{l} \rho u \\ \rho u^2 + p \\ \rho uv \\ \rho uH \end{array} \right|, \qquad \mathbf{G}_1 = \left| \begin{array}{l} \rho v \\ \rho uv \\ \rho v^2 + p \\ \rho vH \end{array} \right|, \qquad \mathbf{Q}_1 = \left| \begin{array}{l} \rho \\ \rho u \\ \rho v \\ e \end{array} \right|.$$

$\mathbf{E}_1$ and $\mathbf{G}_1$ for the two-dimensional Navier–Stokes equations are written as

$$\mathbf{E}_1 = \left| \begin{array}{l} \rho u \\ ru^2 + p + \dfrac{\mu}{\mathrm{Re}_\infty}\left(\dfrac{2}{3}\operatorname{div}\mathbf{V} - \tau_{11}\right) \\ \rho uv - \mu\tau_{12}/\mathrm{Re}_\infty \\ \rho uH + \dfrac{\mu}{\mathrm{Re}_\infty}\left(\dfrac{2}{3}u\operatorname{div}\mathbf{V} - u\tau_{11} - v\tau_{12} - \dfrac{1}{\mathrm{Pr}(\gamma-1)\mathrm{M}_\infty^2}\dfrac{\partial T}{\partial x}\right) \end{array} \right|,$$

$$\mathbf{G}_1 = \left| \begin{array}{l} \rho v \\ \rho vu - \mu\tau_{12}/\mathrm{Re}_\infty \\ \rho v^2 + p + \dfrac{\mu}{\mathrm{Re}_\infty}\left(\dfrac{2}{3}\operatorname{div}\mathbf{V} - \tau_{22}\right) \\ \rho vH + \dfrac{\mu}{\mathrm{Re}_\infty}\left(\dfrac{2}{3}v\operatorname{div}\mathbf{V} - u\tau_{12} - v\tau_{22} - \dfrac{1}{\mathrm{Pr}(\gamma-1)\mathrm{M}_\infty^2}\dfrac{\partial T}{\partial y}\right) \end{array} \right|$$

$$(\tau_{11} = 2\partial u/\partial x, \quad \tau_{12} = \partial u/\partial y + \partial v/\partial x, \quad \tau_{22} = 2\partial v/\partial y, \quad \operatorname{div}\mathbf{V} = \partial u/\partial x + \partial v/\partial y),$$

and the vector $\mathbf{Q}_1$ has the same form as for the Euler equations. Here e is the total energy per unit volume, H is the total enthalpy, p is the pressure, ρ is the density, $\mathbf{V}$ is the velocity vector, u, v are the Cartesian coordinates of the velocity vector, γ is the specific heat ratio, M_∞ is the free-stream Mach number, μ is the dynamic viscosity, and Pr is the Prandtl number.

The system of equations for a perfect gas is closed by the equation of state $p = \rho T/\gamma \mathrm{M}_\infty^2$.

In the Euler and Navier–Stokes equations, the dependent variables are made dimensionless as follows. The Cartesian coordinates are referred to the characteristic length L, the velocity vector is referred to the free-stream velocity, the pressure is referred to the doubled free-stream velocity head, and the other hydrodynamic variables are referred to their free-stream values.

2. In the physical plane, the computation domain is a duct bounded above and below by solid surfaces (Fig. 1). In solving the problem by a fully-implicit method we use the following boundary conditions to close the system of differential equations (1.1).

At the inflow boundary, the following Riemann invariants are used for the Euler and Navier–Stokes equations:

$$A_1 = \frac{2c}{\gamma - 1} - u\frac{\partial \xi}{\partial x} - v\frac{\partial \xi}{\partial y}, \quad A_2 = \frac{p}{\rho^\gamma}, \quad A_3 = v\frac{\partial \xi}{\partial x} - u\frac{\partial \xi}{\partial y}, \quad A_4 = \frac{2c}{\gamma - 1} + u\frac{\partial \xi}{\partial x} + v\frac{\partial \xi}{\partial y},$$

where c is the speed of sound. These invariants correspond to radiation conditions of an outgoing wave. In solving the problem, at each point we analyze the signs of the eigenvalues

$$\lambda_1 = u\frac{\partial\xi}{\partial x} + v\frac{\partial\xi}{\partial y} - c\left(\left(\frac{\partial\xi}{\partial x}\right)^2 + \left(\frac{\partial\xi}{\partial y}\right)^2\right)^{1/2}, \quad \lambda_2 = u\frac{\partial\xi}{\partial x} + v\frac{\partial\xi}{\partial y},$$

$$\lambda_3 = u\frac{\partial\xi}{\partial x} + v\frac{\partial\xi}{\partial y}, \quad \lambda_4 = u\frac{\partial\xi}{\partial x} + v\frac{\partial\xi}{\partial y} + c\left(\left(\frac{\partial\xi}{\partial x}\right)^2 + \left(\frac{\partial\xi}{\partial y}\right)^2\right)^{1/2}.$$

The signs determine the direction of perturbation propagation relative to $\xi = \text{const}$. For $\lambda_i \geqslant 0$, the corresponding invariant is computed from the free-stream gas-dynamic variable values. For $\lambda_i < 0$, linear extrapolation of A_i from the gas-dynamic variable values at interior points of the computation domain is used.

At the outflow boundary, we use "mild" extrapolations of the vector of the desired gas-dynamic variables $\mathbf{F} = (u, v, p, T)^t$ with approximations of the form $3\mathbf{F}_i - 4\mathbf{F}_{i-1} + \mathbf{F}_{i-2} = 0$, instead of extrapolations of the Riemann invariants. As has been shown by numerical experiments, this increases the stability of the iteration process used for the solution of the difference problem and makes it possible to simulate supersonic-flow regimes at the outlet and also some subsonic-flow regimes at the outlet.

For the Euler equations on the upper and lower surfaces, we use extrapolation of the tangential velocity component V_τ in the form $V_\tau^{i+1} - 2V_\tau^i + V_\tau^{i-1} = 0$ ($V_\tau = u$ at the upper boundary; $V_\tau = u\cos\sigma + v\sin\sigma$ on the lower boundary, and σ is the local slope of the lower surface), $V_N = 0$ ($V_N = 0$ is the normal component of the velocity vector; $V_N = v$ on the upper boundary, and $V_N = u\sin\sigma - v\cos\sigma$ on the lower boundary), and extrapolation of the pressure with a constant derivative along the normal to the surface ($\partial p/\partial N = 0$), $H = H_\infty$. For the Navier–Stokes equations on the upper and lower surfaces, we use the attachment and nonpenetration conditions $u = v = 0$ and extrapolation of the pressure along the normal to the wall with a constant derivative ($\partial p/\partial N = 0$), $T = T_w$.

3. To generate a computation grid for the two-dimensional problem, we use the integral method of [7], which is based on the Schwarz–Christoffel conformal mapping. The problem of computation-grid generation is reduced to the solution of a discrete integral equation that is completely determined by the duct geometry. After that, grid-point coordinates are computed by simple integration [8]. This implies that it is possible to generate various grids in a duct by a sufficiently fast algebraic method.

In the variables ξ and η, the computation domain has the form of a rectangle and is covered by a uniform grid with given spacings $h_\xi = (\xi_{\max} - \xi_{\min})/N_\xi$ and $h_\eta = (\eta_{\max} - \eta_{\min})/N_\eta$, where N_ξ and N_η is the number of grid points in the longitudinal and transverse directions. The metric coefficients at grid points are evaluated by numerical differentiation formulas.

As Re increases, the thickness of the boundary layer adjacent to the solid surface decreases, and a sufficiently large number of grid points in the longitudinal direction relative to the solid surface is necessary for an accurate resolution of the flow field in this region.

Let us consider first an algorithm of grid refinement in one direction, which is then easily extended to the two-dimensional case. Let several zones $[a_i, a_{i+1}]$, $i = 1, \ldots, N-1$, be distinguished in an interval $[a_1, a_N]$, and let the grid contain M points. It is required to distribute the points among the zones so that a given fraction p_i of the total number of points ($\Sigma p_i = 1$) is found in each zone.

A continuous analog for this discrete problem is formulated without loss of generality as follows. It is required to find a rigorously increasing function $f(\xi)$ which is defined in the interval $[0, 1]$ and takes values a_1 and a_N at points 0 and 1, respectively, and values $(a_i + a_{i+1})/2$, $i = 1, \ldots, N-1$, at points $\xi_{i+1/2} = (\xi_i + \xi_{i+1})/2$, where $\xi_1 = 0$, $\xi_i = \sum_{k=1}^{i-1} p_k$. The function $f(\xi)$ must be sufficiently smooth.

The solution of this problem is not unique. A possible solution is constructed as follows. We consider a function $h(\xi) = df/d\xi$, which is analogous to a grid step in the continuous formulation of the problem. We introduce the notion of the characteristic step of the ith zone: $h_i = (a_{i+1} - a_i)/(\xi_{i+1} - \xi_i)$, $i = 1, \ldots, N-1$. If we integrate a piecewise continuous function $h_*(\xi)$ [$h_*(\xi) = h_i$ for $\xi \in [\xi_i^+, \xi_{i+1}^-]$, $i = 1, \ldots, N-1$], we obtain a function $f_*(\xi)$ that satisfies the conditions of the problem, but is not sufficiently smooth, because, at the

points ξ_i, its derivative has a discontinuity of the first kind.

To eliminate this disadvantage, we replace the discontinuities of the first kind of the function $h_i(\xi)$ at the points ξ_i by a continuous variation of $h(\xi)$ from h_{i-1} to h_i on an interval that contains the point ξ_i $(i = 2, \ldots, N-1)$. For each i, a function that realizes this smooth variation is denoted by $g_i(\xi)$, and the domain of the function is denoted by $[y_1, y_2]$; in this case, $(y_1 + y_2)/2 = \xi_i$. The function $g_i(\xi) - (h_{i-1} + h_i)/2$ must be uneven relative to the point ξ_i. As g we can use the function

$$g_i(\xi) = h_{i-1} + \frac{1}{2}(h_i - h_{i-1})\left[\sin\left(\frac{\pi(\xi - \xi_i)}{y_2 - y_1}\right) + 1\right].$$

The domain of the function g_i is to some extent arbitrary; in our calculations this is determined by the condition $y_2 - y_1 = \min(p_i, p_{i-1})$ for each ξ_i.

The desired function $h(\xi)$ coincides with $h_*(\xi)$ outside the domain of g_i and is continuously extended to g_i in the interval $[y_1, y_2]$. The point-distribution function $f(\xi)$ is obtained by integrating $h(\xi)$ from 0 to ξ. The function $f(\xi)$ is doubly continuously differentiable.

We extend the grid-refinement algorithm to the two-dimensional case. Let a grid that is uniform in the plane (ξ_{ij}, η_{ij}), where $i = 1, \ldots, N_\xi$ and $j = 1, \ldots, N_\eta$, be constructed by conformal mapping. Let a grid (X_{ij}, Y_{ij}), where $i = 1, \ldots, N_X$ and $j = 1, \ldots, N_Y$, correspond to the former grid in the plane (x, y). Suppose it is necessary to change the distribution of grid points in the transverse direction (along η). Let $i = i_0$. For X_{i0j}, Y_{i0j} $(j = 1, \ldots, N_Y)$, we use the above algorithm of one-dimensional-grid refinement over j, and then repeat this procedure for all $i_0 = 1, \ldots, N_X$. The thus-obtained nonuniform grid can be used in calculations. In the plane (ξ, η), the grid is defined by the point number being considered and is uniform.

In the present paper, we choose two zones of thickness $2/\sqrt{\mathrm{Re}}$ near the upper and lower boundaries of the computation domain. After refinement, each of these zones contains 20% of the total number of points in the transverse direction.

4. The following integrointerpolation method is used to construct the difference scheme of our investigation. The difference analogs of conservation laws have the form

$$\frac{\mathbf{Q}^{n+1}_{j,k} - \mathbf{Q}^{n}_{j,k}}{\tau} + \frac{\mathbf{E}^{n+1}_{j+1/2,k} - \mathbf{E}^{n+1}_{j-1/2,k}}{h_\xi} + \frac{\mathbf{G}^{n+1}_{j,k+1/2} - \mathbf{G}^{n+1}_{j,k-1/2}}{h_\eta} = 0,$$

where n is the time-level number; j and k are the point numbers in the ξ and η coordinates, respectively; and τ is the time step. The fully implicit scheme is conservative, i.e., the conservation laws are satisfied even for discontinuous solutions.

To approximate convective flows at half-integer nodal points, we use the Godunov monotone scheme [9] with the following approximate solution of the Riemann problem of discontinuity decay [10]:

$$\mathbf{E}_{j+1/2} = 0.5(\mathbf{E}_L + \mathbf{E}_R - \mathbf{R}\Phi(\lambda)\mathbf{R}^{-1}(\mathbf{Q}_R - \mathbf{Q}_L)).$$

Here

$$\mathbf{Q} = J\begin{vmatrix} \rho \\ \rho u \\ \rho v \\ e \end{vmatrix}; \qquad \Phi(\lambda) = \begin{vmatrix} \Psi(\lambda_1) & 0 & 0 & 0 \\ 0 & \Psi(\lambda_2) & 0 & 0 \\ 0 & 0 & \Psi(\lambda_3) & 0 \\ 0 & 0 & 0 & \Psi(\lambda_4) \end{vmatrix};$$

and $\mathbf{R}$ is a matrix whose columns are the right eigenvectors of the operator $\partial\mathbf{E}/\partial\mathbf{Q}$. The left $\mathbf{Q}_L$ and right $\mathbf{Q}_R$ values of the dependent variables $\mathbf{Q}$ are calculated using the second-order monotone upstream scheme for conservation laws (MUSCL) by the formulas $\mathbf{Q}_L = \mathbf{Q}_i = 0.5\mathbf{g}_i$, $\mathbf{Q}_R = \mathbf{Q}_{j+1} - 0.5\mathbf{g}_{j+1}$, and $\mathbf{g}_j = f(\Delta_{j+1/2}\mathbf{Q}, \Delta_{j-1/2}\mathbf{Q})$. In these calculations, the following function $\Psi(\lambda)$ and the limiter $f(x, y)$ are used:

$$f(x,y) = \min\mathrm{mod}\,(x,y) = \begin{cases} x, & xy > 0 \text{ and } |x| \leqslant |y|, \\ y, & xy > 0 \text{ and } |x| > |y|, \\ 0, & xy \leqslant 0, \end{cases} \qquad \Psi(\lambda) = \begin{cases} |\lambda| & \text{for } |\lambda| \geqslant \varepsilon, \\ (\lambda^2 + \varepsilon^2)/(2\varepsilon) & \text{for } |\lambda| \leqslant \varepsilon \end{cases}$$

Here ε is a small parameter whose value is 0.1 for the Euler equations and 10^{-3} for the Navier–Stokes equations.

To calculate eigenvalues and eigenvectors, we use the Roe method [10] for the approximate solution of the problem of discontinuity decay:

$$c_{LR} = \frac{c_L\sqrt{\rho_L} + c_R\sqrt{\rho_R}}{\sqrt{\rho_L} + \sqrt{\rho_R}}, \quad u_{LR} = \frac{u_L\sqrt{\rho_L} + u_R\sqrt{\rho_R}}{\sqrt{\rho_L} + \sqrt{\rho_R}}, \quad v_{LR} = \frac{v_L\sqrt{\rho_L} + v_R\sqrt{\rho_R}}{\sqrt{\rho_L} + \sqrt{\rho_R}}$$

(the subscripts L and R correspond to the gas-dynamic variable values to the left and right of the half-integer nodal point at which the flow is approximated).

A second-order central difference scheme is used to approximate the diffusion component of the flux vector in the Navier–Stokes equations.

The approximations used for the two-dimensional Euler and Navier–Stokes equations consist, in the general case, of 9 and 13 points, respectively.

Two methods of approximating the convective flux were tested at half-integer nodal points adjacent to the boundaries of the computational domain. The first method introduces a fictitious nodal point outside the computation domain with subsequent computation of the fluxes by the second-order total variation diminishing (TVD) scheme. The gas-dynamic variable values at the point are computed by extrapolation from the computation domain with a constant derivative. The second method uses a nonmonotone two-point centered difference scheme of second-order accuracy.

A comparison of these methods has shown that they yield approximately identical results for the Euler equations (the maximum differences are on the order of 8%). For the Navier–Stokes equations, the second method ensures faster convergence of the iterative process. The fact that the centered difference scheme is nonmonotone is apparently of no importance in the presence of physical viscosity. Since, in this study, we compare the results obtained for the Euler and Navier–Stokes equations, the second method is used in both cases.

The implicit nonlinear difference scheme obtained is unconditionally stable for a linear problem. This makes it possible to find steady-state solutions of difference equations for a single infinitely large time step.

5. The nonlinear system of difference equations obtained by approximation of the differential system (1.1) can be written as $\mathbf{F}(\mathbf{X}) = 0$, where $\mathbf{X}$ is the vector of the unknown variables and $\mathbf{F}$ is a nonlinear grid operator. For the two-dimensional Euler and Navier–Stokes equations, $\dim(\mathbf{F}) = \dim(\mathbf{X}) = 4 \times N_X \times N_Y$.

In the present paper, we used the algorithm $\mathbf{X}_{N+1} = \mathbf{X}_N - \tau_{N+1}\mathbf{D}^{-1}\mathbf{F}(\mathbf{X}_N)$, $\mathbf{D} = \partial\mathbf{F}/\partial\mathbf{X}_N$ to solve this system. This is the modified Newton method with a quadratic convergence rate for $\tau_N = 1$. In the process of numerical solution, the parameter τ_N is defined by the formula [11]

$$\tau_{N+1} = \frac{(\Delta\mathbf{X}_N - \Delta\mathbf{X}_{N-1}, \mathbf{X}_N - \mathbf{X}_{N-1})}{(\Delta\mathbf{X}_N - \Delta\mathbf{X}_{N-1})^2},$$

where $\Delta\mathbf{X}_N$ is a correction vector. As the iterative process converges, $\tau_N \to 1$.

The Jacobian matrix is formed by means of finite increments of the residual vector with respect to the vector of the desired nodal variables. When the Euler equations are approximated by the scheme described above, the operator $\partial\mathbf{F}/\partial\mathbf{X}$ has a sparse block 9-diagonal structure. When the Navier–Stokes equations are approximated, the operator has a 13-diagonal structure. The elementary block of these structures is a 4×4 dense matrix.

The linear algebraic system obtained in each iteration is solved by a direct method of LU factorization (the matrix $\partial\mathbf{F}/\partial\mathbf{X}_N = \mathbf{L} \times \mathbf{U}$, where $\mathbf{L}$ and $\mathbf{U}$ are lower and upper triagonal matrices).

To reduce the total number of arithmetic operations, the sparseness structure of the matrices $\mathbf{L}$ and $\mathbf{U}$ is initially analyzed, and the unknowns are then renumbered by generalized nested dissection [12]. This method has been tested widely in numerical experiments, and its robustness and high effectiveness have been proved [1, 13].

6. The computation domain is a duct of variable cross section (Fig. 1). The height of the duct inlet H_0 is used as the characteristic linear dimension. The relative length of the duct is $l = l^*/H_0 = 4$, and the relative length of the inlet is $l_{\text{in}} = 1$. The transition from the inlet to a duct section of lower height ("throat" with $h_{\text{throat}} = 0.75$) is realized in a region with length $l_t - 1 = 0.6869$ with constant wall slope of $\theta = 20°$.

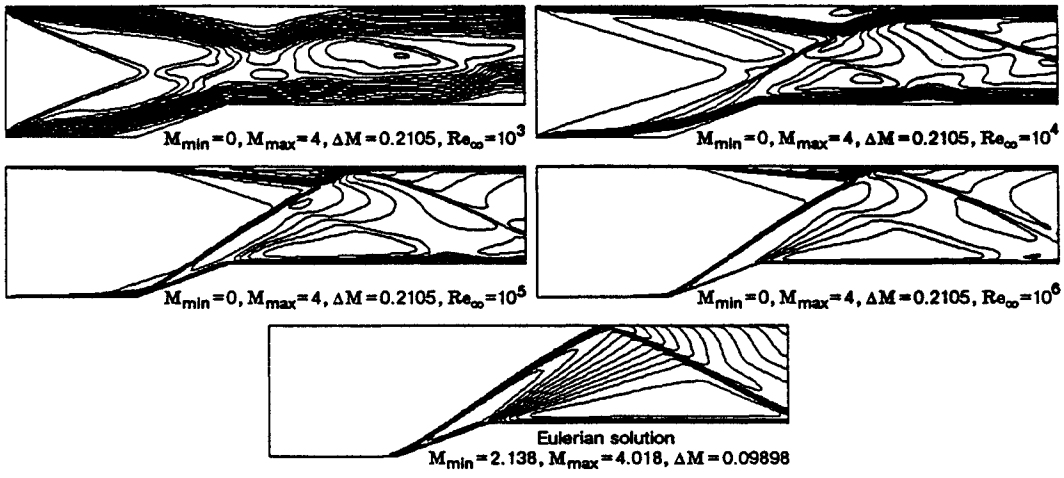

Fig. 2

The relative length of the "throat" is $l_{throat} = 2.3131$ or, relative to the throat size, $l_{throat}/h_{throat} = 3.08$.

The computations are performed at a constant duct-inlet Mach number $M_\infty = 4.0$ for an ideal and viscous perfect gas with specific heat ratio $\gamma = 1.4$, Prandtl number $Pr = 0.7$, and with dynamic viscosity that is an exponential function of temperature ($\mu \sim T^{0.7}$). The streamlined surfaces are assumed to be isothermal with a temperature factor $T_{w0} = T_w/T_0 = 0.5$, where $T_0 = 1+0.5(\gamma-1)M_\infty^2$ is the temperature of free-stream retardation.

The viscous-gas variant ($Re_\infty = 1000$, $M_\infty = 4$, and $T_{w0} = 0.5$) is computed on 101×61 and 101×121 grids to estimate the computation-grid effect on the modeling results. Comparison of the results has shown that they differ by only 1–2% in regions in which the variables have extrema [6]. This suggests that, for the problem considered, a 101×61 grid resolves fairly well all features of the flow field, and its further refinement does not introduce large quantitative changes into the results.

In spite of this, all the results in the present paper are obtained on a 101×101 grid by using a second-order monotone scheme to provide for the best resolution for the extrema of the desired functions. The average CPU time for each variant is 0.8 h on an RS-6000 work station.

7. The various isoline patterns and tomograms obtained for the flat duct give a general idea of the flow structure and the effects of the Reynolds number. As an example, Fig. 2 gives isoline patterns of M = const, and Fig. 3 shows tomograms of the temperature field.

For the smallest Reynolds number used ($Re_\infty = 10^3$), the internal-friction forces manifest themselves over the entire flow field. The perturbations from the inlet edges caused by a thick boundary layer propagate downstream as shock waves and are confined to a comparatively small free-stream region at the inlet. The flows at the lower and upper surfaces begin to interact at $x \approx 1$, i.e., the perturbed flows attach at a distance of the order of the characteristic linear dimension.

In the perturbed flow field, thick boundary layers, which leave almost no place for the inviscid core of the flow, hardly allow one to distinguish the interacting shock-wave contours. The flow past the wedge-shaped surface separates. The resulting shock waves interact with the upper surface, forming a broad bounded region of separation, and leave the computation domain after reflection. On the upper surface in the flow past the separated zone, a shock wave forms which is incident on the lower surface, causes flow separation, and, after reflection, leaves the computation domain.

As Re increases, the boundary layers thin down, and the perturbations from the inlet edges gradually degenerate into Mach lines. This leads to an increase in the inlet area, the "inviscid" flow core increases, and the system of interacting shock waves becomes more pronounced. The separated flow regions remain, move along the duct, and vary in size.

For the greatest Re numbers, the flow structure is very close to the flow structure of an ideal gas. In this case, on the lower surface of the duct, separated flow regions are almost unnoticeable, whereas on the

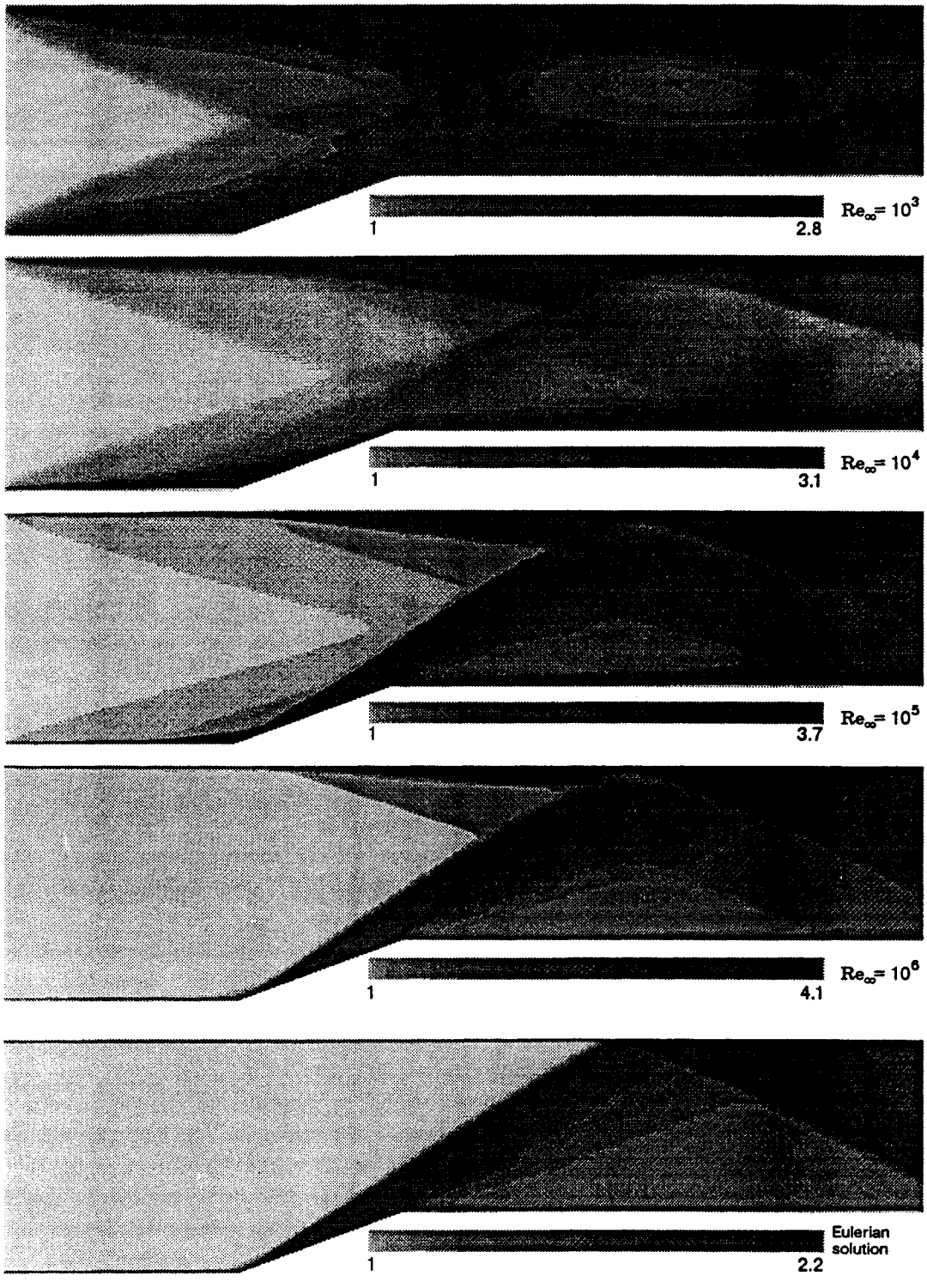
$Re_\infty = 10^3$
1
2.8
$Re_\infty = 10^4$
1
3.1
$Re_\infty = 10^5$
1
3.7
$Re_\infty = 10^6$
1
4.1
Eulerian solution
1
2.2

Fig. 3

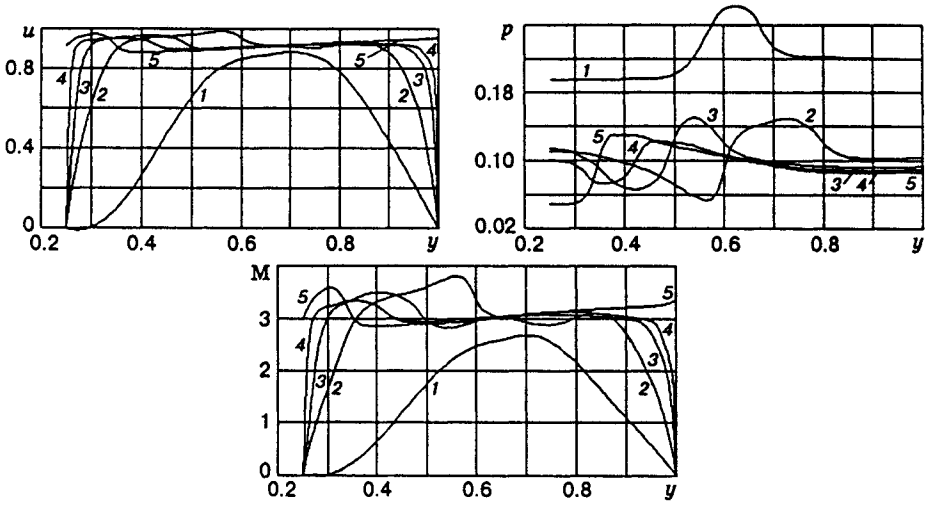

Fig. 4

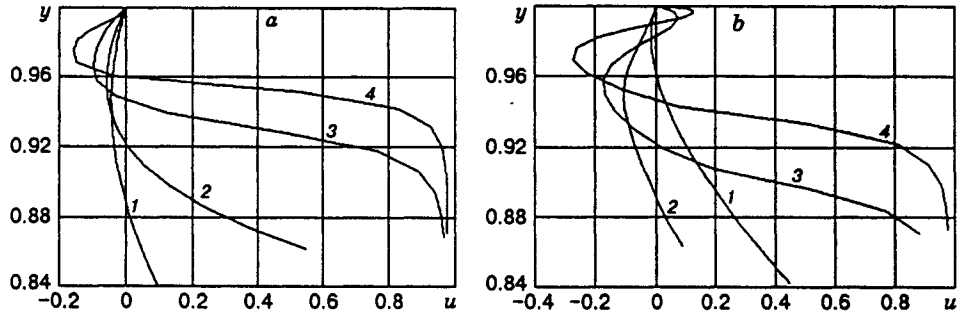

Fig. 5

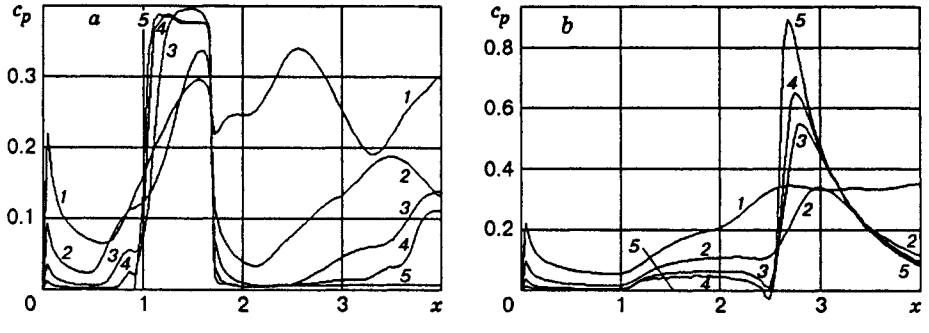

Fig. 6

TABLE 1

Re_∞	Lower surface			Upper surface		
	x_S	x_R	Δ_S	x_S	x_R	Δ_S
10^3	0.944	1.063	0.119	1.35	2.42	1.07
	3.64	—	—			
$3 \cdot 10^3$	0.80	1.283	0.483	1.302	2.69	1.388
	2.61	2.80	0.19			
10^4	0.66	1.387	0.727	1.237	2.87	1.633
	2.72	3.275	0.555			
$3 \cdot 10^4$	0.647	1.311	0.664	1.207	2.84	1.633
	2.747	3.604	0.857	2.400	2.2	0.20
10^5	0.729	1.186	0.457	1.167	2.773	1.606
	2.981	3.768	0.787	2.438	2.143	0.295
$3 \cdot 10^5$	0.781	1.131	0.35	1.118	2.756	1.638
	3.170	3.756	0.586	2.437	2.0	0.437
10^6	0.837	1.077	0.24	1.123	2.746	1.623
	3.368	3.802	0.434	2.484	1.917	0.567

upper surface, a broad bounded separation flow region caused by the interaction of a shock wave with the boundary layer is observed.

The isoline patterns and tomograms do not show a detailed structure of the separated zones. This structure is determined by analysis of the other flow characteristics.

8. An analysis of the profiles of gas-dynamic variables for various cross sections of the duct gives the following useful information.

In cross section 1–1, the profiles of gas-dynamic variables are strongly perturbed and already affected by the wedge-shaped surface in the vicinity of the lower surface. As a result, profiles are no longer symmetric about the axis of the duct. The flow past the corner point is separated here for all Re considered. As Re increases, the core of the inviscid flow increases in size and coincides with the free stream (as is the case within the framework of the Euler equations).

In cross section 2–2 (the "throat" inlet), the profiles of gas-dynamic variables indicate the formation of a "classical" profile as Re increases. This profile is initially strongly perturbed and then becomes stepwise as the shock wave passes through cross section 2–2. The profiles also indicate that for all flow regimes, the flow past the corner point of the "throat" is not separated.

For cross section 3–3 (the intermediate cross section of the "throat"), the profiles are strongly perturbed, and are in agreement with the Euler profile in the central part.

For cross section 4–4 (the outlet cross-section of the "throat" in Fig. 4, where curves 1–4 correspond to $Re_\infty = 10^3$, 10^4, 10^5, and 10^6, and curve 5 corresponds to inviscid flow), the profiles of gas-dynamic variables are strongly perturbed, since the reflected shock waves leave the computation domain for the "throat" sizes considered. In this case, even for the largest Re, the profiles of gas-dynamic variables differ from the Euler solution because of the differences in the flow structure, i.e., in the Euler solution, the outlet cross section is intersected by a single shock wave, while, in the viscid solution, it is intersected by two shock waves.

As was noted above, a broad bounded area of separated flow forms on the upper surface of the duct. As an illustration of the structure of this region, Fig. 5 shows a series of profiles of the longitudinal-velocity component in the wall layer versus Re_∞ for two cross sections [$x = 1.539$ (a) and 2.308 (b), curves 1–4 correspond to $Re_\infty = 10^3$, 10^4, 10^5, and 10^6]. For the inlet cross section (Fig. 5a) of the separated region, the velocity profiles are of the same type for all Re. For the cross section (Fig. 5b) in the central part of the separated region, the type of velocity profile changes with an increase Re. This indicates that at large Re, conditions for flow reseparation and reattachment are created in the separated region.

9. The distribution of the pressure coefficient c_p on the upper and lower surfaces of the duct (Fig. 6a refers to the lower surface and Fig. 6b to the upper surface; curves 1–4 correspond to $Re_\infty = 10^3$, 10^4, 10^5,

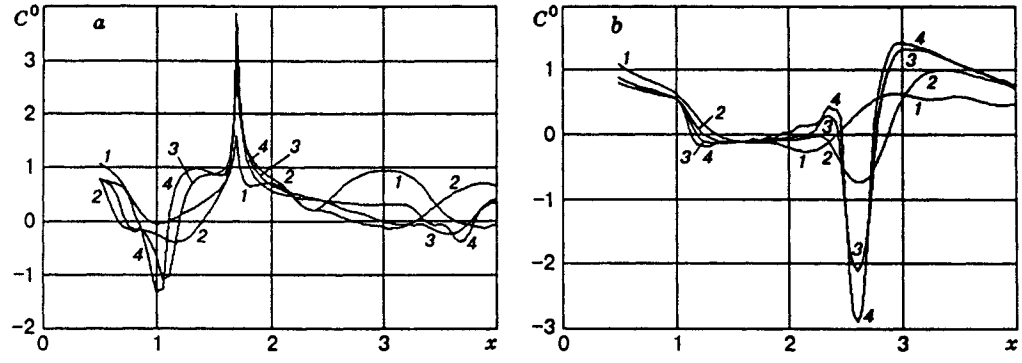

Fig. 7

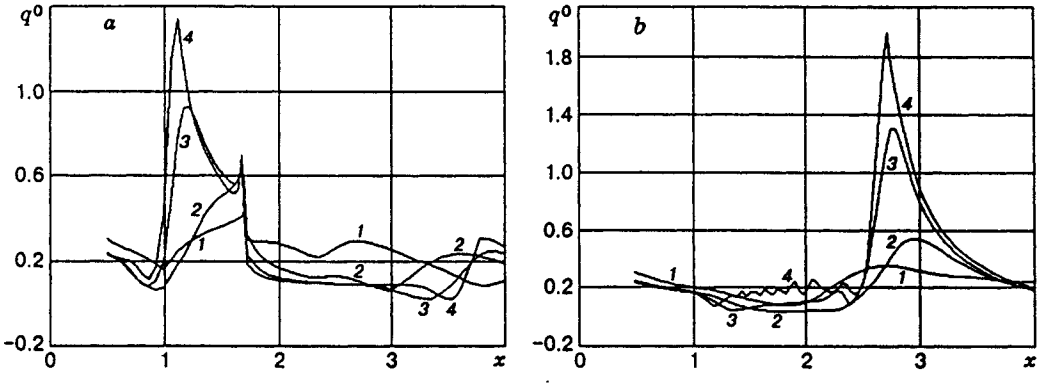

Fig. 8

and 10^6, and curve 5 corresponds to inviscid flow) shows once again that as the Reynolds number increases, the distribution of c_p basically approaches the Euler solution. Some local differences, however, remain. They are caused by the internal-friction forces. In the vicinity of the inlet edges of the duct, the pressure coefficient increases as $x \to 0$. It must increase infinitely when the attachment condition is satisfied for the Navier–Stokes equations. In the viscous flow adjacent to the lower wall, the first local pressure maximum is located on the wedge-shaped surface. In addition, the second local pressure maximum forms in the "throat" of the duct. At large Re, this maximum is located downstream behind the reattachment point.

On the upper surface, the absolute pressure maximum forms in the region of interaction of a shock wave with the boundary layer. Further downstream, the pressure decreases monotonically under the effect of the expansion fan caused by the corner point of the "throat." The pressure "plateau" ahead of the maximum, i.e., the region in which the pressure is nearly constant, indicates the presence of a developed separated flow region.

The distributions of the skin friction coefficient $C_f = \tau_w/(0.5\rho_\infty V_\infty^2)$ over the upper and lower duct surfaces [Fig. 7, where $C^0 = C_f\sqrt{\mathrm{Re}_\infty}$, curves 1–4 correspond to $\mathrm{Re}_\infty = 10^3$, 10^4, 10^5, and 10^6, (a) refers to the lower surface, and (b) refers to the upper surface] make it possible to determine the detailed structure of the separated flow regions.

These distributions show clearly that two closed regions of separated flow form on the lower surface of the duct. One region is located in the flow past the wedge vertex, and the other is located in the "throat" of the duct near the outlet cross section.

Some geometrical characteristics of the separated zones are given in Table 1. Here x_S and x_R are the separation and reattachment points, respectively, and $\Delta_S = x_R - x_S$ is the length of the separated region. As Re increases, the separation points on the lower surface first move upstream and then downstream. The

lengths of the separated zones also vary in a nonmonotone fashion.

The interpretation of the structure of the separated zones on the lower surface is evident and does not involve difficulties, whereas the situation on the upper surface of the duct is different. Additional information on the velocity field (see Fig. 5) is required to determine the structure of the separated zones and to interpret correctly the friction-stress distribution. From this it follows that a single broad closed separated flow area forms on the upper surface for all values of Re. As Re increases, however, conditions are created in this zone that lead to flow reseparation and reattachment.

It should be noted that as the Reynolds number increases ($\mathrm{Re}_\infty > 10^4$), the lengths of the separated zones adjacent to the lower surface decrease, and the length of the separated zone adjacent to the upper surface is stabilized. Hence, we can conclude that, although with an increase in Re the flow field approaches the Euler solution, it never reaches it. The limiting form of the viscous solution for $\mathrm{Re}_\infty \to \infty$ apparently contains a closed zone of reversed flow adjacent to the upper surface of the duct.

The distributions of the local heat flux q_w^* over the lower and upper surfaces of the duct are shown in Fig. 8, where $q^0 = q_w\sqrt{\mathrm{Re}_\infty}$, $q_w = q_w^*/(0.5\rho_\infty V_\infty^3)$, curves 1–4 correspond to $\mathrm{Re}_\infty = 10^3$, 10^4, 10^5, and 10^6, (a) refers to the lower surface, and (b) refers to the upper surface. The complex structure of the flow field is responsible for the complicated nonmonotone behavior of the heat flux on the streamlined surfaces. On the upper surface, the primary maximum of the heat flux is formed in the region of interaction of a shock wave with the boundary layer. This maximum is located downstream behind the reattachment point. On the lower surface, several local maxima of the heat flux with comparable magnitudes are observed. The sharpest of these maxima is located at the corner point of the "throat." The second maximum is located near the outlet cross section of the "throat" behind the flow reattachment point. The magnitude of this maximum depends almost not at all on Re. The third maximum is located on the wedge-shaped surface behind the flow reattachment point. This maximum appears and becomes predominant at large values of Re.

The friction-stress and heat-flux distributions show that, for large Re numbers, there are oscillations in the numerical solution for the upper surface of the duct in the separated region. The amplitudes of these oscillations increase with an increase in Re. This phenomenon is likely caused by the physical instability of the laminar separated flow.

This work was supported by the Russian Foundation for Fundamental Research (Grant 95–01–01129a).

REFERENCES

1. I. V. Egorov and O. L. Zaitsev, "One approach to the numerical solution of the two-dimensional Navier–Stokes equations by the shock capturing method," *Zh. Vychisl. Mat. Mat. Fiz.*, **31**, No. 2, 286–299 (1991).
2. V. A. Bashkin, I. V. Yegorov, and M. V. Yegorova, "A circular cylinder in the supersonic flow of a perfect gas," *Izv. Ross. Akad. Nauk, Mekh. Zhidk. Gaza*, No. 6, 107–115 (1993).
3. V. A. Bashkin, I. V. Egorov, and N. P. Kolina, "Aerodynamic characteristics of axisymmetric nosed bodies in supersonic flow," *Uch. Zap. TsAGI*, **24**, No. 2, 44–53 (1993).
4. I. V. Egorov, "On the question of the influence of the real properties of air on integral aerodynamic characteristics," *Izv. Ross. Akad. Nauk, Mekh. Zhidk. Gaza*, No. 4, 156–164 (1992).
5. V. A. Bashkin and I. V. Yegorov, "The heat-transfer numerical simulation on the basis of Navier–Stokes equations," in: *Research in Hypersonic Flows and Hypersonic Technologies*, TsAGI, September 19–21 (1994), Section 2, pp. 12–16.
6. I. V. Egorov and D. V. Ivanov, "Use of fully-implicit monotone difference schemes to simulate plane internal flows," *Zh. Vychisl. Mat. Mat. Fiz.*, **36**, No. 10 (1996).
7. A. E. Vnukov, "Generation of computation grids around aerodynamic profiles using the Schwarz–Christoffel discrete transformation," Preprint No. 35, TsAGI, Moscow (1991).
8. R. W. MacCormack, "The effect of viscosity in hypervelocity impact cratering," AIAA Paper No. 354, New York (1969).

9. S. K. Godunov, "A finite-difference method for numerical computation of discontinuous solutions of the equations of fluid dynamics," *Mat. Sb.*, **47**, No. 3, 271–306 (1959).
10. P. L. Roe, "Approximate Riemann solvers, parameter vectors, and difference schemes," *J. Comput. Phys.*, **43**, 357–372 (1981).
11. T. Kh. Karimov, "Some iterative methods for solving nonlinear equations in Hilbert space," *Dokl. Akad. Nauk SSSR*, **269**, No. 5, 1038–1042 (1983).
12. R. J. Lipton, D. J. Rose, and R. E. Tarjan, "Generalized nested dissection," *SIAM J. Numer. Anal.*, **16**, No. 2, 346–358 (1979).
13. I. V. Egorov and O. L. Zaitsev, "Development of efficient algorithms for computational fluid dynamic problems," in: *Proc. of the 5th Int. Symp. on Computational Fluid Dynamics*, Sendai, Japan (1993), Vol. 3, pp. 393–400.